energies

MDPI

Article

Numerical Simulation of the Thermal Performance of a Microchannel Heat Sink with Variable-Height Fins in Counter-Flow Mode

Chang-Qiang Hu, Jia-Jia Yu, Chun-Mei Wu and You-Rong Li *

School of Energy and Power Engineering, Chongqing University, Chongqing 400044, China
* Correspondence: liyourong@cqu.edu.cn

Abstract

In this paper, a novel heat sink with variable-height fins under a counter-flow configuration was proposed and its thermal performance was systematically investigated by three-dimensional numerical simulation. The primary objective was to optimize the thermal performance of microchannel heat sinks through the modification of flow arrangements and fin structural design. The results reveal that the counter-flow arrangement can significantly reduce the maximum base temperature, form a centrally symmetric temperature field, and enhance the uniformity of the base surface temperature. Among all proposed variable-height fin schemes, the linearly rising–descending-height fin (LRDHF) model can effectively reduce the peak temperature and enhance the temperature uniformity of the base surface. Under the conditions of a heat flux of $q_w = 2.5 \times 10^6$ W/m^2 and $Re = 200$, the minimum base temperature and the absolute average temperature difference can be reduced to 339.9 K and 0.65 K, respectively. Parametric analysis indicates that at a fixed heat transfer area, increasing the channel width while decreasing the channel height deteriorates the thermal performance of microchannel heat sinks. In addition, high-accuracy empirical correlations for flow and heat transfer applicable to the LRDHF model considered in this work are established, with the average errors of the friction factor and Nusselt number correlations not exceeding 10% and 8%, respectively. This study verifies the synergistic benefits of integrating a streamwise variable-height fin structure with a counter-flow arrangement, offering an effective optimization strategy for the design of high-performance microchannel heat sinks.

Keywords: microchannel heat sink; counter flow; variable-height fins; performance evaluation; temperature uniformity

Check for updates

Academic Editor: Mahmoud Bourouis

Received: 5 September 2026
Revised: 16 October 2026
Accepted: 22 October 2026
Published: 24 October 2026

Copyright: © 2026 by the authors. Licensee MDPI, Basel, Switzerland. This article is an open access article distributed under the terms and conditions of the Creative Commons Attribution (CC BY) license.

1. Introduction

The rapid development of semiconductor technology and escalating market demands for high-performance electronics have driven remarkable increases in device integration density. Consequently, thermal power densities in electronic devices have risen sharply, rendering thermal management a critical bottleneck for system reliability and longevity. Heat sink performance has a considerable impact on operational stability and the service life of electronic devices. Microchannel heat sinks have emerged as a promising solution for high-flux thermal management in compact electronic systems [1], owing to their superior packaging compatibility with densely integrated components and exceptionally high surface-to-volume ratios that enable efficient heat dissipation. Among the various

enhancement techniques for microchannel heat sinks, the integration of fins arranged in specific patterns within channels has garnered considerable attention due to its substantial potential for heat transfer augmentation.

Extensive studies have demonstrated that fin geometry exerts profound influences on the thermo-hydraulic characteristics of microchannels [2–4]. For instance, staggered petal-shaped fin configurations have been shown to effectively mitigate localized hot spot temperatures [5], arranging clover-shaped ribs on the sidewalls of microchannels can substantially enhance the enhancement factor at high Reynolds numbers [6], and so on. Bio-inspired design has emerged as a powerful paradigm for addressing complex engineering challenges. This biomimetic approach has found extensive applications in microchannel heat sink design, and the resulting designs exhibit better thermo-hydraulic behavior than their conventional straight-channel counterparts. By drawing inspiration from efficient transport networks, optimized surface structures, or unique fluid control mechanisms found in organisms, researchers can design microchannel configurations with superior thermo-hydraulic performance. Based on the above conditions, researchers have proposed a series of microchannel heat sinks with biomimetic structures [7–10]. It has been found that the performance of microchannel heat sinks with biomimetic structures improved compared to straight-channel designs.

However, microchannel heat sinks with biomimetic structures often involve complex geometries, which make them difficult to fabricate and impose certain limitations on their practical application. Therefore, current efforts on structural optimization of microchannel heat sinks remain focused on conventional configurations, including modifications to channel geometry and fin architecture. Some researchers have proposed arranging symmetric pointed-arch ribs on the wall surfaces of microchannel heat sinks to improve thermal performance with a minimal increase in pressure drop [11]. The fin structure was optimized by creating secondary flow channels inside regular hexagonal prism fins to enhance heat transfer [12]. To improve heat transfer and fluid mixing between the mainstream and the near-wall flow, a twisted blade-shaped fin was proposed [13]. Research has shown that different fin specifications have varying effects on flow and heat transfer [14]. Some researchers have conducted studies on fins with various shapes and have comprehensively compared the thermo-hydraulic performance of fins with different geometries [15].

Temperature uniformity is another critical performance metric in microchannel heat sink design. Temperature gradients within the heat sink can induce thermomechanical stresses, which in turn reduce device reliability and may even shorten operational lifetime. To improve temperature uniformity, researchers have introduced various microstructures into microchannels, including ribs [16], cavities [17–19], vortex generators [20,21], and secondary flow channels [22,23]. Numerous studies have confirmed that these structures can improve the temperature uniformity of the base surface effectively.

Structural gradient variation is an effective approach to improving temperature uniformity. Shen et al. [24] optimized vertical bifurcation positions in channel centers, while Feng et al. [25] developed embedded gradient-distributed pin–fin arrays. Alternatively, streamwise-varying fin density has been designed to accommodate thermal boundary layer evolution along the flow direction [26]. Li et al. [27] proposed a manifold-distributed array jet heat sink with four lateral outlets to investigate its improvement in temperature uniformity. Li et al. [28] improved the temperature uniformity of microchannel heat sinks by varying the shapes and arrangements of fins. It has been demonstrated that fin thickness significantly affects the heat transfer and fluid flow characteristics of microchannel heat sinks [29]. Studies have shown that varying the geometric structure of microchannel heat sinks along the flow direction is also an effective approach to improving their heat dissipation performance [30–32]. Beyond geometric modifications, flow arrangement significantly

affects temperature distribution [33–37]. These collective efforts underscore the growing research emphasis on temperature uniformity optimization [38,39].

Despite extensive research on microchannel heat sinks, existing structural optimization strategies have been predominantly confined to three domains, including channel geometry, fin shape and height, all implemented under the conventional parallel-flow arrangement. Within this framework, two critical issues remain conspicuously under-addressed. First, the potential of streamwise non-uniform fin configurations which could theoretically compensate for the progressive deterioration in streamwise local heat transfer coefficient has not been systematically exploited. Second, the thermo-hydraulic characteristics of counter-flow configurations have received little attention, despite their inherent advantage in promoting temperature uniformity through interchannel thermal coupling.

To address these issues, the present study proposes a counter-flow microchannel heat sink equipped with streamwise variable-height fins. This design is underpinned by a dual-mechanism rationale: the streamwise height gradation of the fins enables adaptive matching of the decaying local thermal demand, while the counter-flow arrangement establishes a centrosymmetric thermal field that effectively relocates the hot spot to the central region, thereby circumventing the exit-side overheating inherent to parallel-flow systems. This work bears some similarity to the study in Ref. [40]; however, the latter did not specifically investigate the influence of the height variation range on the performance of microchannel heat sinks. The present study delves deeper into this aspect and, unlike Ref. [40], is conducted under counter-flow conditions, so as to further investigate the synergy between variable-height fins and the counter-flow mode, which also constitutes the novelty of this work.

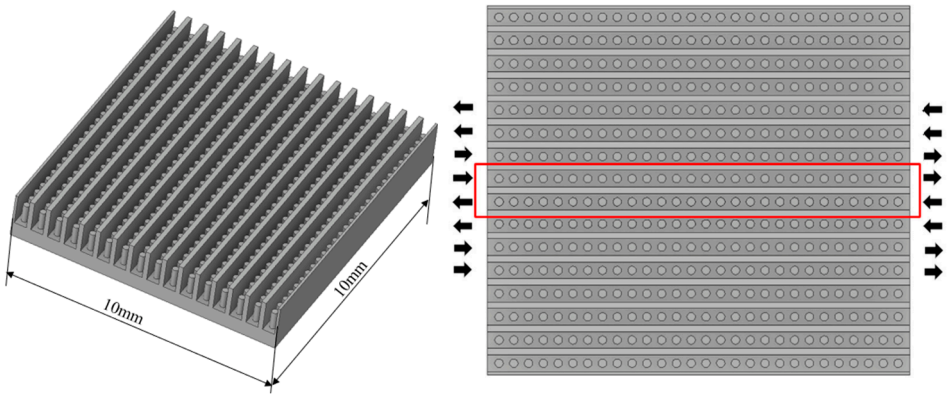
2. Theoretical Model

2.1. Physical Model

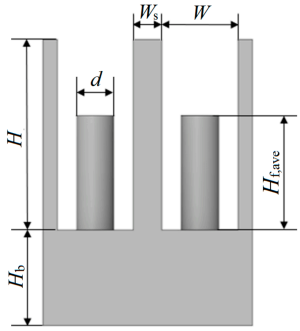
Figure 1 illustrates the geometric model and computational domain in the red box of the proposed microchannel heat sink, The arrows in Figure 1a indicate the direction of the coolant flow. Specifically, Figure 1a displays the full-scale model of the uniform-height fin microchannel heat sink and illustrates the selection of the computational unit, while Figure 1b details the dimensional parameters of the computational unit. In Figure 1, H represents the channel height, H_b denotes the base thickness, d refers to the fin diameter, W_s is the sidewall thickness, W stands for the channel width, and $H_{f,ave}$ corresponds to the average fin height.

The computational domain is defined as a unit consisting of two adjacent channels with opposite flow directions. This simplification is adopted because lateral thermal interaction between channels with identical flow directions is negligible, such that the boundaries between adjacent units can be treated as adiabatic. Such a domain reduction strategy significantly reduces computational cost while faithfully retaining the key thermo-hydraulic features of the full counter-flow configuration. Since the computational model is not a complete multichannel heat sink, it cannot reproduce the phenomenon of non-uniform flow distribution. Therefore, this study has the limitation of neglecting the non-uniform flow distribution in multichannel heat sinks.

Table 1 lists the main parameters of the microchannel heat sink, where W_s represents the full sidewall thickness, and the wall thickness on both sides of the computational domain is half of the sidewall thickness. H denotes the channel height, W denotes the channel width, and H_b denotes the base thickness.



(**a**) Geometric model and computational domain in the red box



(**b**) Dimensional annotation

Figure 1. Geometric model and computational domain of microchannel.

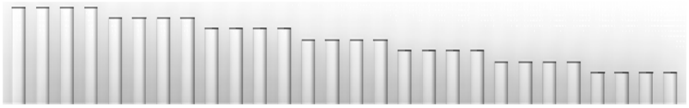
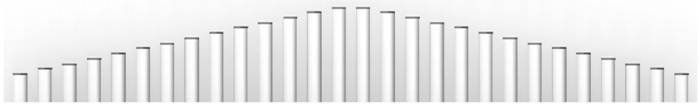
Table 1. The main dimensional parameters of the microchannel.

Geometric parameters	W	W_s	H	H_b	d
mm	0.4	0.15	1	0.5	0.2

To thoroughly investigate the influence of streamwise fin height variation on thermo-hydraulic performance, five distinct fin configurations are examined, as shown in Table 2. The uniform-height fin (UHF) configuration serves as the reference case, with all variable-height designs maintaining identical total fin surface areas to ensure equitable performance comparison. With a constant fin diameter and count across all configurations, the equal cumulative fin height ensures an identical transfer area. The fin height of the uniform-height fin is 0.6 mm. For the linearly rising/descending-height fins (LRHF/LDHF), the fin height increases/decreases linearly in the flow direction. For the stepwise rising/descending-height fins (SRHF/SDHF), the fin height increases/decreases linearly in a stepwise manner with every four fins as a unit. For the linearly rising-descending-height fin (LRDHF), the fin height increases linearly along the flow direction until reaching the maximum value, and then decreases linearly with an identical slope.

On this basis, the thermal–hydraulic performance of each variable-height fin model is investigated under different height variation ranges, with the fin area kept constant. Since the height varies linearly for all models, maintaining a constant heat transfer area requires only that the average of the minimum and maximum fin heights ($H_{f,min}$ and $H_{f,max}$) equals the height of a uniform-height fin of $H_{f,ave} = (H_{f,min} + H_{f,max})/2 = 0.6$ mm.

Table 2. Schematic of fin height variation along flow direction.

No.	Model	Fin Configuration
0	UHF	
1	LRHF	
2	LDHF	
3	SRHF	
4	SDHF	
5	LRDHF	

2.2. Mathematical Model

The numerical simulation is conducted under the following assumptions: (1) The working fluid is incompressible water. (2) The range of Reynolds (*Re*) numbers is from 200 to 600. Therefore, the flow is laminar and steady, with conjugate heat transfer. (3) The copper is adopted as the solid heat sink material, and its thermophysical properties are constant. However, the thermophysical parameters of water are considered to be temperature-dependent. (4) Natural convection and viscous dissipation are assumed to be neglected.

Based on the above assumptions, the governing equations are presented as follows:

Continuity equation:

$$\nabla \cdot (\rho_{\mathbf{f}} V) = 0. \tag{1}$$

Momentum equation:

$$V \cdot \nabla(\rho_{\mathbf{f}} V) = -\nabla P + \nabla \cdot (\mu_{\mathbf{f}} \nabla V). \tag{2}$$

Energy equation for the fluid domain:

$$V \cdot \nabla(\rho_{\mathbf{f}} c_{p_{\mathbf{f}}} T_{\mathbf{f}}) = \nabla \cdot (k_{\mathbf{f}} \nabla T_{\mathbf{f}}). \tag{3}$$

Energy equation for the solid domain:

$$\nabla \cdot (k_{\mathrm{s}} \nabla T_{\mathrm{s}}) = 0. \tag{4}$$

where $\boldsymbol{V}$ is the velocity vector, ρ is the density, μ is the dynamic viscosity, c_{p} is the specific heat capacity at constant pressure, T is the temperature, and k is the thermal conductivity. The subscripts "f" and "s" represent the fluid and solid, respectively.

The polynomial expressions for the temperature-dependent thermophysical properties of water in the temperature range of 5 °C to 95 °C are given by [40]

$$\rho = 765.33 + 1.8142T - 0.0035T^2, \tag{5}$$

$$c_p = 28070 - 281.7T + 1.25T^2 - 2.48 \times 10^{-3}T^3 + 1.857 \times 10^{-6}T^4, \tag{6}$$

$$\lambda = -0.5752 + 6.397 \times 10^{-3}T - 8.151 \times 10^{-6}T^2, \tag{7}$$

$$\mu = 9.67 \times 10^{-2} - 8.207 \times 10^{-4}T + 2.344 \times 10^{-6}T^2 - 2.244 \times 10^{-9}T^3. \tag{8}$$

The fluid inlet is assigned a velocity inlet condition at a fixed temperature of T_o = 293 K, with the velocity magnitude tailored to achieve the target Reynolds number. A pressure outlet condition with zero gauge pressure is applied at the outlet, and no-slip conditions are enforced along all solid–fluid interfaces. A uniform heat flux of $q_w = 2.5 \times 10^6$ W/m^2 is imposed on the bottom wall, with the top and sidewalls thermally insulated. This heat flux is representative for high-power electronic devices. For all investigated cases under this heat flux, the fluid temperature stays below the saturation temperature under the corresponding pressure, and single-phase flow is preserved.

The convective heat transfer coefficient h is calculated as

$$h = \frac{q_e}{T_{w,ave} - T_{f,ave}}, \tag{9}$$

where $T_{w,ave}$ is the average temperature of the solid–fluid interface, $T_{f,ave}$ is the mean temperature of the fluid, and q_e is the effective heat flux, which is given by

$$q_e = q_w \frac{A_w}{A_e}, \tag{10}$$

where q_w is the heat flux applied at the base surface of the microchannel, which is maintained at a constant value. $A_w = 2(W + W_s)L$ is the base area of the unit microchannel, where L is the length of the channel. $A_e = 2[(2H + W)L + \pi d n H_{f,ave} + n\pi d^2/4]$ is the solid–fluid interface area in contact with the fluid, and n denotes the number of fins within a single channel.

Reynolds (Re) number is the independent variable, which is defined as

$$Re = \frac{\rho_f u D}{\mu_f}, \tag{11}$$

where u is the fluid inlet velocity and D is the characteristic length of the channel, $D = 2WH/(W + H)$.

After the pressure drop ΔP is determined, the friction factor is calculated as follows

$$f = \frac{D\Delta P}{2L\rho_f u_m^2}. \tag{12}$$

The Nusselt (Nu) number is defined as

$$Nu = hD/\lambda_f. \tag{13}$$

2.3. Numerical Method and Validation

Numerical simulations are performed using the commercial software ANSYS Fluent 2022 R1, which is based on the finite volume method, to analyze the three-dimensional conjugate heat transfer and the flow characteristics in microchannels with different micro-fin configurations. Geometric modeling is conducted in ANSYS SpaceClaim 2022 R1,

and mesh generation is accomplished using ANSYS Meshing 2022 R1, with structured hexahedral meshes adopted and local refinement applied in the near-wall regions. The pressure–velocity coupling is handled by the SIMPLE algorithm, the convective term is discretized using the second-order upwind scheme, and the resulting linear system of equations is solved using the Gauss–Seidel method. The convergence criteria for the continuity, momentum, and energy equations are set to residuals of 10^{-6}, 10^{-3}, and 10^{-6}, respectively. Convergence is considered to be achieved when the monitored values of relevant physical quantities at the inlet and outlet remain stable and all residuals fall below the specified thresholds.

2.4. Grid Independency Test

Grid independence validation was conducted based on the average Nusselt number and pressure drop for each model at Re = 200. The models examined include UHF, LRHF and SRHF with fin height varying from 0.3 to 0.9 mm. As shown in Table 3, four sets of grids were employed with mesh density increasing sequentially. Using the finest grid (Set 4) as the reference, the relative deviations for Set 3 are all within 1%. Therefore, grid-independent results were achieved with Set 3, which was subsequently employed for all simulations.

Table 3. Grid independence check for UHF, LRHF and SRHF at Re = 200.

Model	Set	Mesh Density	*Nu*	Relative Deviation, %	Δ*P*	Relative Deviation, %
UHF	Set1	446,032	16.76	1.63	1264.09	1.61
	Set2	891,873	17.10	0.33	1257.38	1.07
	Set3	1,322,030	17.08	0.23	1251.93	0.63
	Set4	2,167,223	17.04		1244.10	
LRHF	Set1	446,585	18.18	1.723	1613.13	1.26
	Set2	889,530	18.58	0.455	1652.72	1.18
	Set3	1,325,542	18.50	0.0243	1649.80	1
	Set4	2,163,817	18.50		1633.52	
SRHF	Set1	447,030	20.96	4	1792.10	1.50
	Set2	890,189	21.59	1.1	1784.34	1.06
	Set3	1,325,345	21.65	0.83	1763.99	0.088
	Set4	2,164,944	21.83		1765.54	

2.5. Model Validation

Numerical model validation was performed using simulation data from Ref. [40] for both the UHF and LDHF models. Validation results are presented in Figure 2. Within the range of Re = 200–800, the calculated Nu and ΔP for both the UHF and LDHF models agree with the literature data to within 5% deviation.

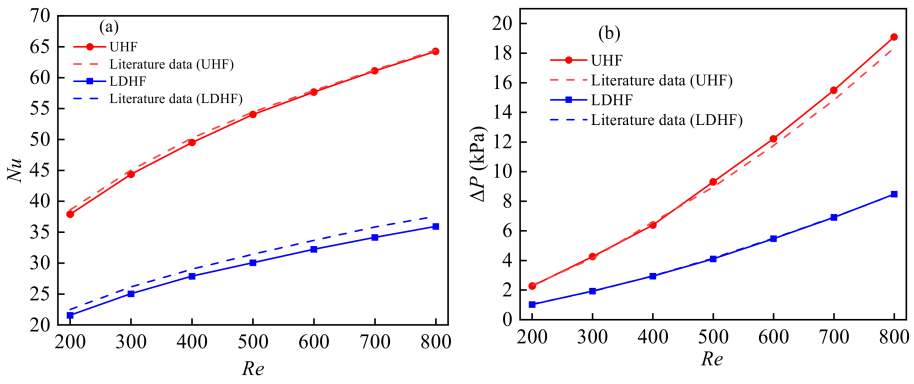


Figure 2. Comparisons of Nu (**a**) and ΔP (**b**) for both UHF and LDHF with the results from Ref. [40] at $q = 2.5 \times 10^6$ W/m^2.

The experimental pressure drop (ΔP) and the temperature variation (ΔT) in water between the microchannel inlet and outlet reported in Ref. [41] are employed for validation at $q = 10^6$ W/m^2. The results are presented in Figure 3. It can be found that both the predicted temperature variation in cooling water between the inlet and outlet and the pressure drop show close agreement with the measured values at $200 \leq Re \leq 500$. The larger discrepancies are observed at $Re > 500$, but these deviations fall within the bounds imposed by the inherent experimental measurement uncertainties.

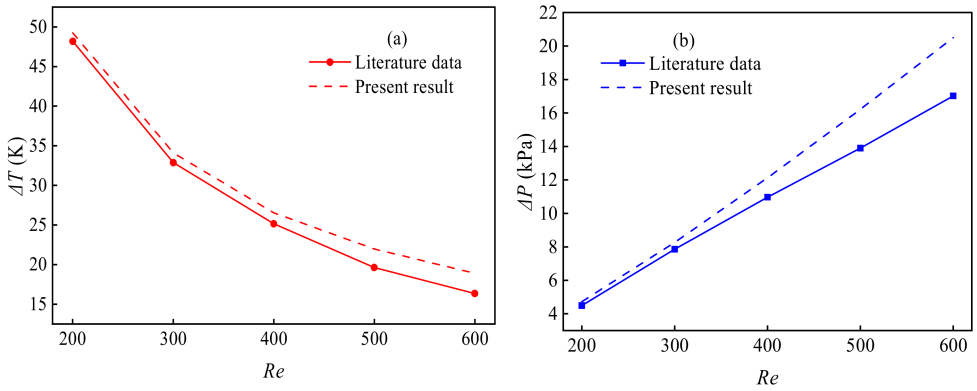


Figure 3. Comparisons of the temperature variation (**a**) in water between the inlet and outlet and the pressure drop (**b**) with the experimental results from Ref. [41] at $q = 10^6$ W/m^2.

Figure 4 compares the numerically predicted Nusselt number and friction factor with the experimental data from Ref. [42] for the MC-RPF model at $q = 10^6$ W/m^2 when the Reynolds number varies from 200 to 600. The maximum deviations for the Nusselt number and the friction factor are 9.8% and 7.6%, respectively, both of which are within the acceptable range.

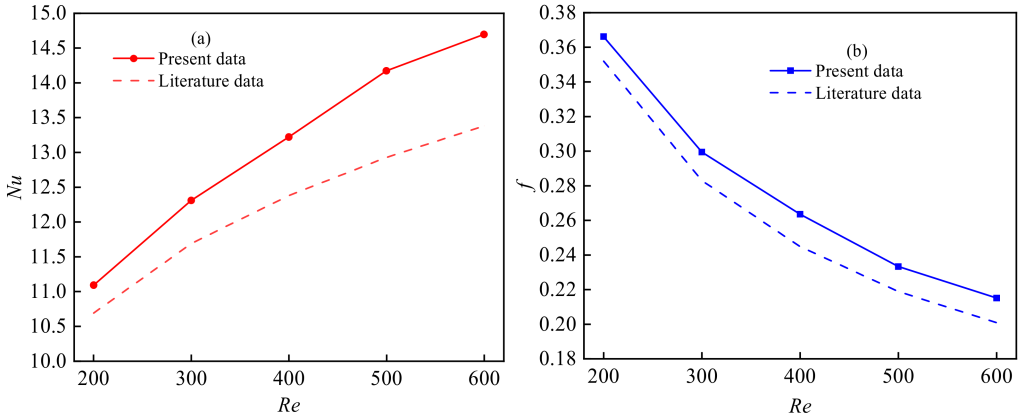


Figure 4. Comparison of the numerically predicted Nusselt number (**a**) and friction factor (**b**) with the experimental data from Ref. [42] for the MC-RPF model at $q = 10^6$ W/m^2.

Based on the above validation results, the mathematical model and simulation method employed in this work can be considered reliable.

3. Results and Discussion

3.1. Comparison of Parallel and Counter Flows

Coolant flow arrangements in microchannel heat sinks are primarily categorized into parallel and counter flows. In a parallel-flow configuration, the coolant flows in the same direction across all channels, whereas a counter-flow configuration features opposite flow directions in adjacent channels, leading to distinct thermo-hydraulic performance

characteristics for the two arrangements. Parallel flow facilitates simplified pumping system layouts but suffers from a substantial temperature increase along the flow path. By contrast, counter flow provides a larger fluid–solid temperature difference for heat transfer enhancement, though it requires a more complex pumping layout. This study presents a comprehensive comparative analysis of the pressure drop and heat transfer characteristics of these two flow configurations.

Figure 5 compares the bottom surface temperature distributions of parallel-flow and counter-flow configurations for UHF at Re = 200(The arrows denote the coolant flow direction, and this applies to all subsequent contour plots). A notable streamwise temperature gradient is seen in parallel-flow mode, while the counter-flow mode yields a relatively symmetric temperature field with the hot spot concentrated near the central region. In addition, the parallel-flow configuration exhibits a higher maximum bottom temperature compared with the counter-flow counterpart. These results indicate that the counter-flow configuration achieves a lower peak substrate temperature and a centrosymmetric temperature distribution, enabling more effective and uniform temperature regulation of the microchannel heat sink.

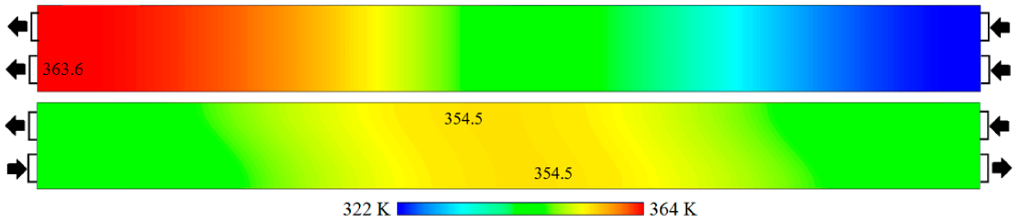


Figure 5. Temperature contours on the base surface of parallel (upper) and counter (lower) flows for UHF configurations at Re = 200.

Figure 6 presents the maximum bottom surface temperature (T_{max}) and the maximum temperature difference (ΔT_{max}) across the base surface for the UHF configurations with counter-flow and parallel-flow arrangements. Over the range of Re = 200–600, the counter-flow arrangement exhibits a lower maximum base surface temperature and a smaller maximum temperature difference across the base surface compared to the parallel-flow arrangement. The maximum base surface temperature difference is defined as

$$\Delta T_{max} = T_{max} - T_{min}, \tag{14}$$

where T_{min} denotes the lowest temperature on the bottom surface.

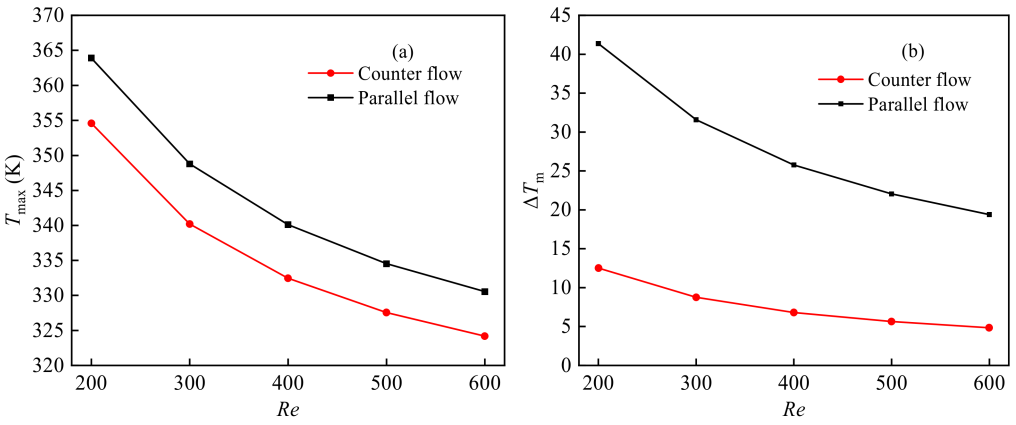


Figure 6. Comparisons of T_{max} (**a**) and ΔT_{max} (**b**) between parallel and counter flows for UHF con figurations.

The underlying mechanism for the reduced highest temperature and maximum temperature difference in the counter-flow mode can be explained as follows: In this configuration, the inlet and outlet are located on opposite sides. As the coolant flows along the channel, heat is absorbed and thus its temperature rises progressively. This heated coolant then exchanges heat with the cooler coolant in the adjacent channel through the solid fin wall. This thermal interaction allows the hot coolant to partially release heat, thereby reducing its own temperature and re-establishing a larger heat transfer temperature difference between the coolant and the channel wall for enhanced heat transfer. Specifically, the temperature distribution in the counter-flow mode exhibits the following characteristics: upon entering the channel, the coolant is preheated by exchanging heat with the adjacent channel, resulting in a temperature rise; during the latter half of the cooling process, it is cooled by exchanging heat with the adjacent channel, leading to a temperature reduction. Consequently, the maximum temperature appears at the midsection of the channel. By contrast, the parallel-flow mode exhibits negligible lateral heat transfer between adjacent channels, causing the coolant temperature to rise continuously in the streamwise direction, with the maximum temperature occurring at the outlet. Therefore, the counter-flow mode demonstrates a lower maximum temperature, a higher minimum temperature at the inlet, and a centrally symmetric temperature distribution.

From the perspective of the obtained results, the counter-flow mode demonstrates significant advantages for temperature control scenarios required by contemporary electronic devices. Relative to parallel flow, the counter-flow configuration not only achieves a lower maximum temperature of the base surface but also significantly reduces the temperature difference on the base surface while exhibiting a centrally symmetric temperature distribution. The combination of lower peak temperature, reduced temperature gradient, and symmetric temperature profile facilitates more precise temperature control and thermal management.

The maximum bottom surface temperatures for both parallel and counter-flow arrangements decrease with increasing *Re*, following a consistent downward trend. However, the variations in the maximum base surface temperature difference with *Re* exhibit distinct behaviors between the two configurations. The parallel-flow mode undergoes a rapid decline as *Re* increases, whereas the counter-flow mode shows a more gradual decreasing trend (see Figure 6). This discrepancy arises because, in the parallel-flow configuration, the base surface temperature rises monotonically in the flow direction. In contrast, for the counter-flow configuration, heat is exchanged not only between the coolant and the vertical channel walls, but also between fluids in adjacent channels via the transverse separating walls. Consequently, the temperature variation in the counter-flow mode is more spatially confined, making the impact of *Re* on the base surface temperature distribution less pronounced than that in the parallel-flow case.

3.2. Effect of Varying Fin Height

3.2.1. Flow Pressure Drop

Over the entire investigated range of fin heights, variable-height fins yield a larger pressure drop compared with uniform-height fins (UHFs), as shown in Figure 7. For the UHF, the periodically varying flow cross-sectional area renders the pressure drop as being dominated primarily by shape drag. But variable-height fins experience continuous flow velocity fluctuations induced by the change in the flow passage cross-section, which introduces additional flow resistance. Flow contraction takes place as fluid travels from low-fin-height to high-fin-height regions, reducing the cross-section of the flow path and accelerating the bulk flow, which further induces contraction losses. Conversely, flow expansion occurs in the reverse flow direction, enlarging the cross-sectional area and decelerating the bulk flow; this process yields expansion losses and triggers flow separation additionally.

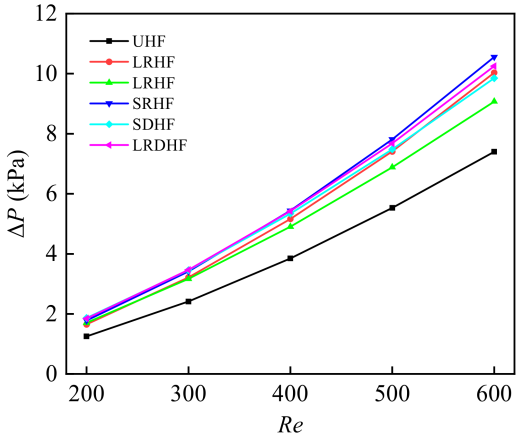


Figure 7. Pressure drop of the variable-height fin models at a fin height variation from 0.3 mm to 0.9 mm.

Figures 8 and 9 present the pressure contours and velocity contours on planes perpendicular to the channel bottom surface for UHF, LRHF, SRHF, and LRDHF, respectively, where the fin heights of LRHF, SRHF, and LRDHF vary from 0.3 to 0.9 mm. As can be seen from Figure 8, the inlet pressure of the UHF is lower than that of the LRHF, SRHF, and LRDHF models. Combined with the velocity contours in Figure 9, the fluid velocity between the fins of the UHF model is almost zero, whereas noticeable fluid velocity exists between the fins of the variable-height fin models. This indicates that the fluid mixing near the fins is enhanced when the fluid flows through the variable-height fin models, thereby improving the heat transfer performance. Moreover, it can be observed that the variation in the flow passage cross-sectional area along the flow direction leads to a considerable velocity variation along the flow direction in the variable-height models. The smaller the flow passage cross-sectional area, the higher the flow velocity, the stronger the fluid mixing, and consequently the stronger the heat transfer.

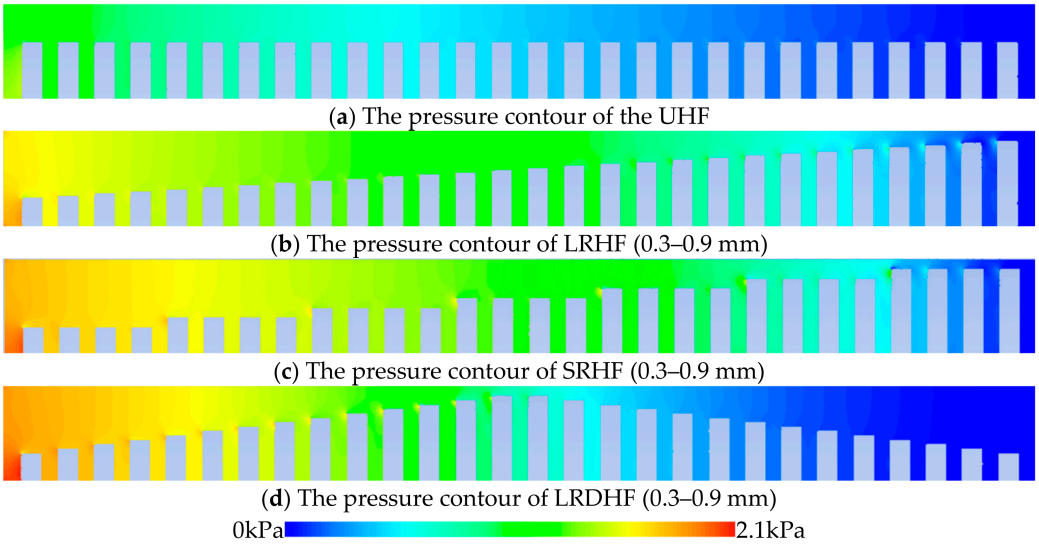


Figure 8. Pressure contours on planes perpendicular to the channel bottom surface for UHF (**a**), LRHF (0.3–0.9 mm) (**b**), SRHF (0.3–0.9 mm) (**c**), and LRDHF (0.3–0.9 mm) (**d**).

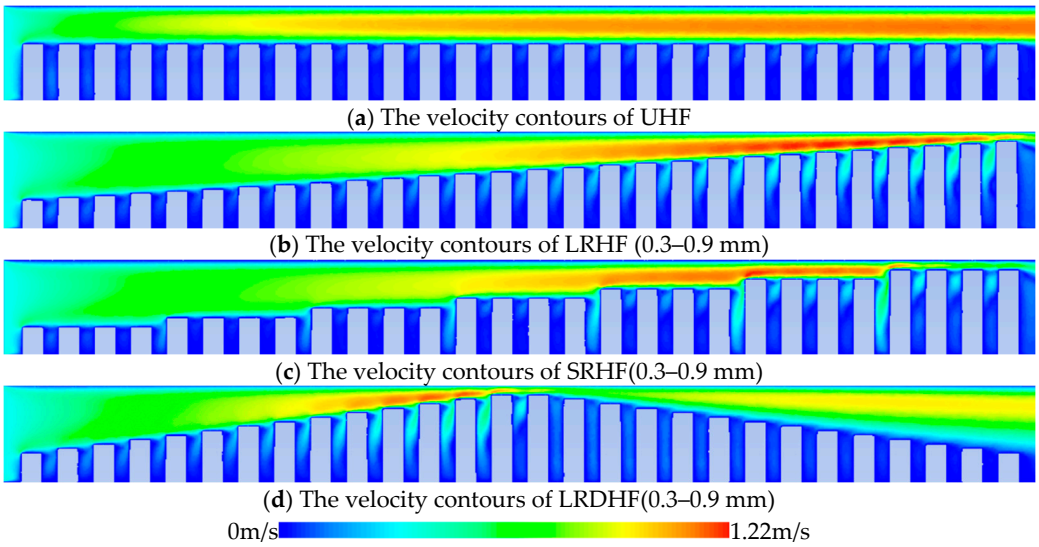


Figure 9. Velocity contours on planes perpendicular to the channel bottom surface for UHF, LRHF (0.3–0.9 mm), SRHF (0.3–0.9 mm), and LRDHF (0.3–0.9 mm).

Figure 10 presents a comparison of the three types of variable-height models with those in Ref. [40]. Even though the flow mode and the height variation range are different, they exhibit the same trend: under identical operating conditions, the pressure drop of the variable-height fin models is larger than that of the uniform-height fin model, and the pressure drops of the LRDHF and LRHF models within the same height variation range are relatively close under the same boundary conditions, which agrees well with the literature. The difference lies in the fact that, under the same conditions, the pressure drop gap between LRDHF and LRHF in this study is somewhat larger. This difference is related to the flow mode and the height variation, as the present study adopts counter flow while the flow modes in the literature are all parallel flow. This further demonstrates the rationality of the research methodology adopted in this study.

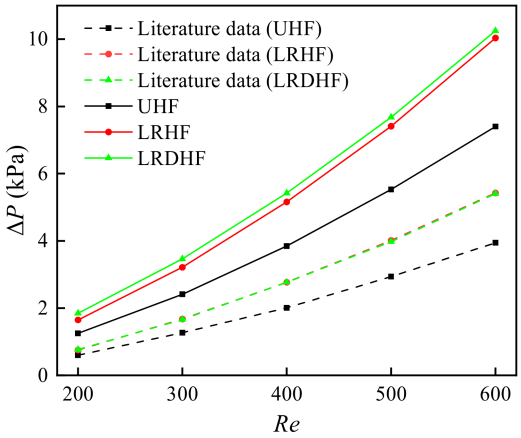


Figure 10. Comparison of the trends of UHF, LRHF, and LRDHF with those in Ref. [40] as a function of *Re*.

3.2.2. Thermal Performance

As shown in Figure 11a, under the condition of a fixed fin heat transfer area, all variable-height fins yield lower peak base temperatures than UHF across the entire height variation range, indicating that the streamwise fin height variation enhances heat transfer. This reduction originates from the intensified disturbance of the coolant induced by the variable-height fins. In addition, vertical-direction disturbances generated within these

channels promote fluid mixing. The combined enhancement of disturbance and mixing consequently increases the convective heat transfer coefficient, which consequently results in a reduction in the maximum base surface temperature.

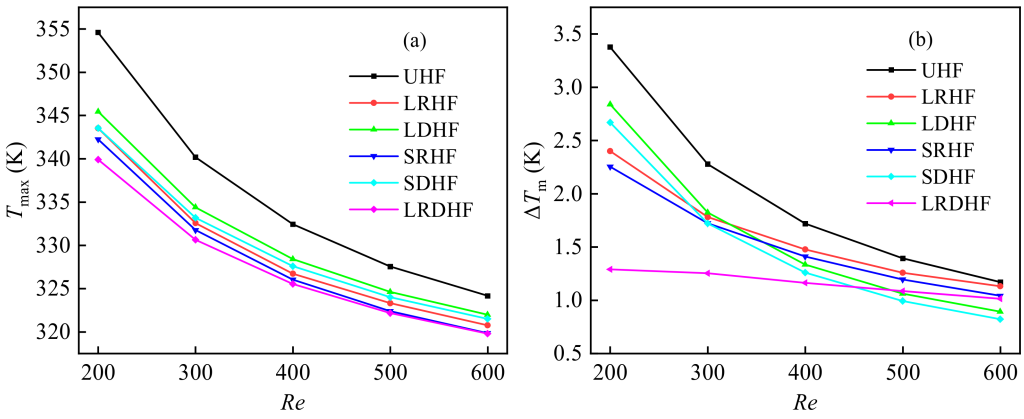


Figure 11. The maximum base temperature (**a**) and absolute mean temperature (**b**) difference for the variable-height fin models at a fin height variation from 0.3 mm to 0.9 mm.

As shown in Figure 11b, the absolute mean temperature difference in base surface for all variable-height fin models under the maximum height variation range is smaller than that of UHF, indicating that the varying fin height along flow direction lowers the peak base surface temperature and enhances the uniformity of temperature. Absolute mean temperature difference is defined as:

$$\Delta T_{\mathrm{m}} = \frac{1}{A}\int_{A} |T - T_{\mathrm{ave}}| \mathrm{d}A, \tag{15}$$

where T represents the temperature on the base surface and T_{ave} is the average temperature. This expression represents the average deviation in the local surface temperature from its mean value over the base surface, and a smaller value indicates better temperature uniformity.

The entrance effect produces enhanced heat transfer in the entry region relative to the average heat transfer level in the channel, owing to the incompletely developed and extremely thin thermal boundary layer in this region. This characteristic generates an exceedingly large near-wall temperature gradient, which contributes to the superior capability of heat transfer in the entry section. Given the intrinsically high heat transfer intensity in the entrance region, the variation in fin height exerts a marginal influence on local thermal performance. As the fluid proceeds along the flow path, its temperature rises continuously owing to persistent heat absorption. For counter-flow operating conditions, the fluid temperature peaks at the channel midpoint and subsequently decreases. A streamwise linear increase in fin height effectively compensates for this thermal performance degradation. As the flow develops into the fully developed regime, the deterioration in heat transfer due to the diminishing fluid–solid temperature difference is partially offset by the progressively enlarged area of heat transfer supplied by the rising fin height. For both LDHF and SDHF configurations, higher fin height in the entrance region further strengthens the already enhanced thermal performance in the entrance region. Although such thermal augmentation gradually decays in the streamwise direction, the robust heat transfer level maintained in the upstream half sufficiently compensates for the performance deterioration occurring in the further downstream region.

The LRDHF configuration achieves the optimal fin height layout for thermal performance under counter-flow conditions. Characterized by low fins at both the inlet and outlet and high fins in the midchannel region, this unique layout well matches the streamwise

temperature evolution of the coolant, which increases from the inlet to the channel midpoint in counter-flow systems progressively. For UHF structures operating under counter-flow conditions, the fluid peak temperature occurs in the midchannel region, where the capability of local heat transfer is weakest. Therefore, the arrangement of tall fins in this middle section provides the maximum available heat transfer area at the position with the minimum heat transfer temperature difference from the base to the fluid. This design adaptively conforms to the spatial variation in fluid thermal characteristics and realizes a good match between the channel structure and heat transfer conditions.

Figure 12 illustrates the base surface temperature contours of different fin models with a fin height variation ranging from 0.3 to 0.9 mm at Re = 200. It is evident that all variable-height fin configurations yield a lower maximum base temperature compared with the UHF counterpart, with the locations of peak temperatures explicitly labeled in the figure. Apart from the LRDHF model, all other configurations exhibit nearly identical distributions of hot and cold temperature zones. In contrast, the LRDHF model presents a distinctly different base temperature distribution, where hot zones appear on both lateral sides rather than concentrating in the central channel region. This is due to the dominant thermal enhancement induced by the enlarged heat transfer area in the midchannel region. The beneficial effect of area augmentation substantially offsets the adverse impact of the reduced fluid–solid temperature difference, ultimately lowering the temperature in the central zone.

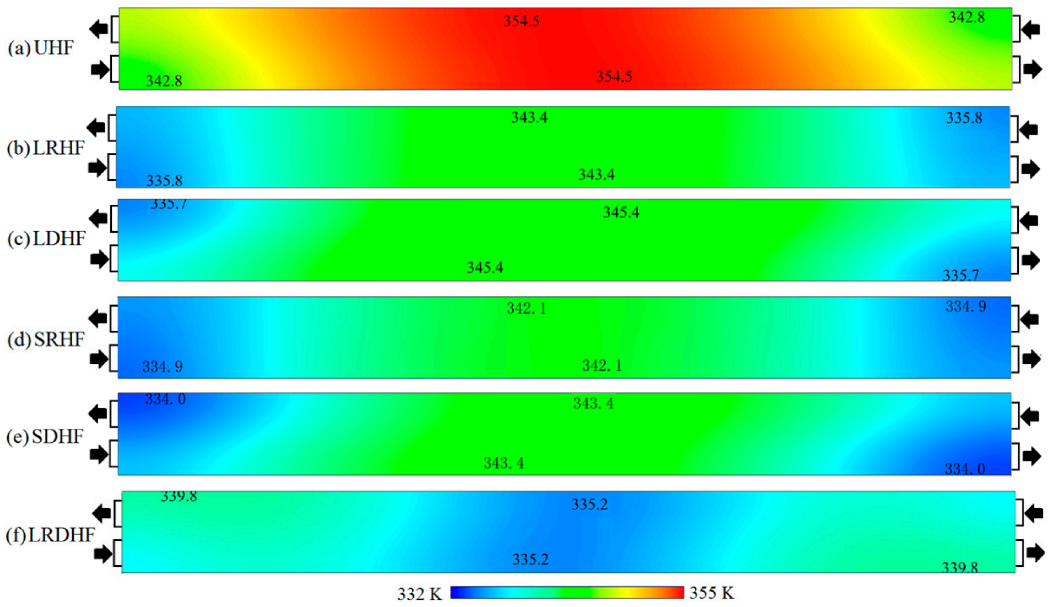


Figure 12. The base surface temperature contours of various models with a fin height variation ranging from 0.3 to 0.9 mm at Re = 200.

3.2.3. Comprehensive Performance

Overall, under identical operating conditions, streamwise rising-height fins deliver a lower maximum base temperature than descending-height fins, while incurring a higher pressure drop. But streamwise descending-height fins achieve a lower absolute mean temperature difference under the same operating conditions, while exhibiting a higher maximum base temperature than their rising-height counterparts. The LRDHF configuration produces the minimum T_{max} among all tested fin layouts. Moreover, it achieves the best temperature uniformity at low Re and presents a weaker variation in thermal uniformity with increasing Re compared with the other models, despite its relatively high pressure drop. Although the UHF configuration features a favorable low pressure drop, its inferior

thermal performance makes it unsuitable for high-heat-dissipation applications and it is thus far from an optimal design choice.

Figure 13a depicts the maximum base temperature of various variable-fin-height models under different fin height variation ranges at Re = 200. The maximum base temperature increases as the fin height variation range decreases, with the UHF configuration yielding the maximum value. The magnitude of thermal enhancement is positively correlated with the degree of fin height variation, demonstrating that a slight modification in fin height geometry can enhance the heat transfer performance significantly. As the height variation range decreases, the increment in the maximum base temperature becomes more prominent for streamwise rising-height fin configurations, whereas descending-height fins exhibit a relatively mild variation. The LRDHF configuration maintains the lowest maximum base temperature across all three height variation scenarios, further validating its superior heat transfer augmentation capability. Under identical height variation ranges, distinct differences in the maximum base temperature are observed among various variable-height fin models, indicating that, for a fixed total fin area, rational spatial distribution of fin area is crucial in determining the overall thermal performance.

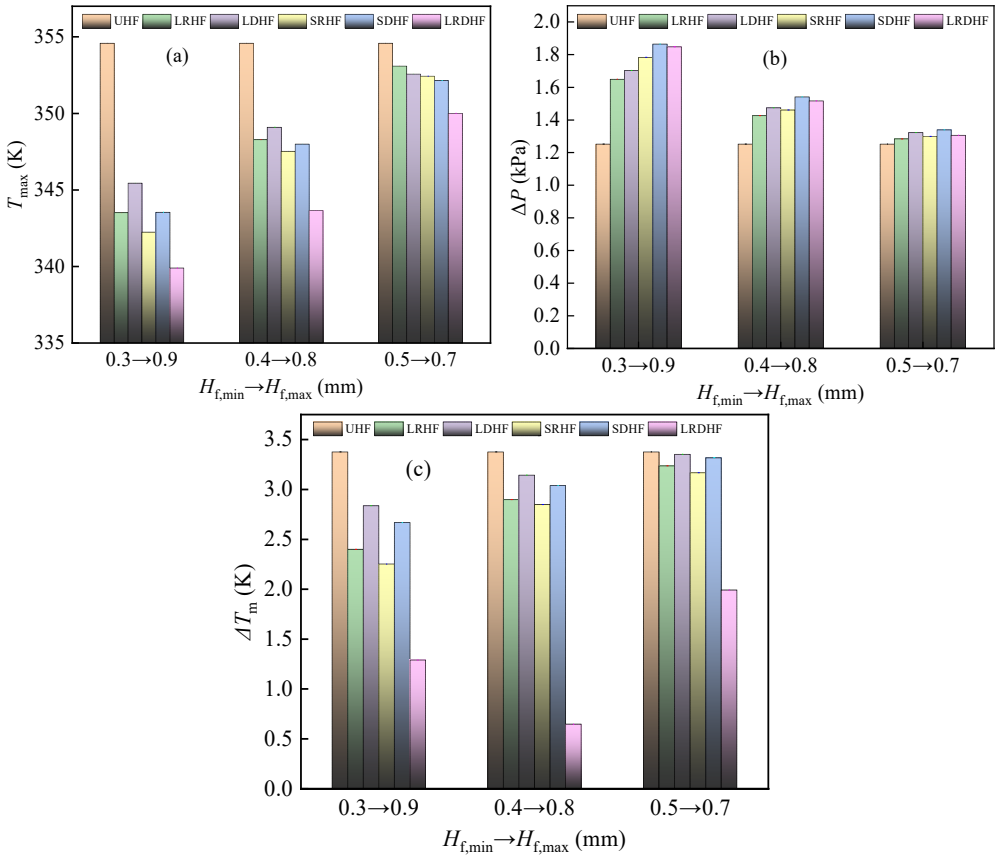


Figure 13. The maximum temperature (**a**), channel pressure drop (**b**), and absolute mean temperature difference (**c**) on the base surface at different fin height variation ranges.

Figure 13b shows the pressure drop of various variable-fin-height models under different fin height variation ranges at Re = 200. All variable-height fin configurations produce a higher ΔP than their UHF counterpart across the three investigated variation ranges, which align with the well-recognized trade-off principle in microchannel thermal systems that heat transfer augmentation is invariably accompanied by a higher ΔP penalty. A larger fin height variation range contributes to a reduced maximum base temperature,

yet simultaneously induces a higher flow pressure drop, revealing a typical performance balance between thermal improvement and pressure drop penalty.

Figure 13c illustrates the absolute mean temperature differences in the base surface for various variable-fin-height models with different height variation ranges at Re = 200. All variable-height fin configurations exhibit a lower absolute mean temperature difference than the UHF case across the three investigated variation ranges, demonstrating that streamwise variable-height fin arrangements can enhance the temperature uniformity of the base surface significantly. In addition, the temperature uniformity deteriorates gradually as the fin height variation range decreases.

Figure 14 compares the Nusselt number of the UHF configuration and three LRDHF configurations with different fin height variation ranges at $200 \leq Re \leq 600$. All LRDHF configurations yield higher Nu than the baseline UHF. The 0.5–0.7 mm case provides a relatively modest enhancement in heat transfer, while the 0.4–0.8 mm case achieves a more pronounced enhancement. However, when the height variation range is further widened to 0.3–0.9 mm, the heat transfer gain no longer continues to rise, and the enhancement effect instead declines somewhat.

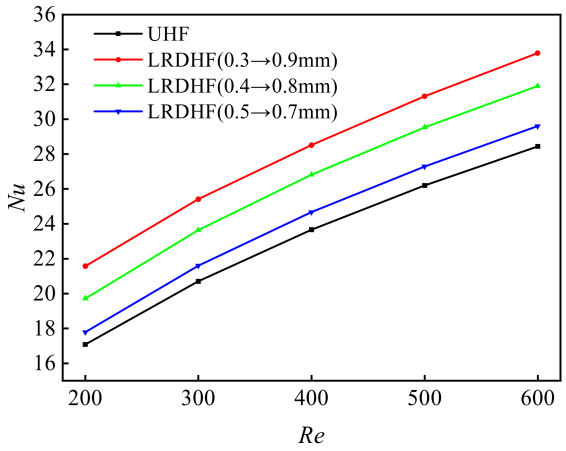


Figure 14. Comparison of *Nu* for the LRDHF with three distinct fin height variation ranges.

Figure 15 presents the maximum bottom surface temperature (a) and the pressure drop (b) of the LRDHF model under three fin height variation ranges. As can be seen from (a), under the same height variation range, the maximum bottom surface temperature in the counter-flow case is consistently lower than that in the parallel-flow case. Moreover, the maximum bottom surface temperature in the parallel-flow case increases as the height variation range decreases, which is consistent with the trend observed under the counter-flow condition. Furthermore, under identical boundary conditions, the difference in the maximum bottom surface temperature between the counter-flow and parallel-flow cases of the uniform-height fin model is further amplified in the variable-height fin model, indicating that the combination of counter-flow operation and variable-height fins further enhances the heat transfer performance, i.e., a synergistic effect is generated. As can be seen from (b), there is almost no difference in pressure drop between the counter-flow and parallel-flow models within the same height variation range. This is because the primary factor governing the pressure drop is the channel geometry. For the same model, the variation in pressure drop caused by changing the flow pattern originates from the difference in fluid viscosity induced by different fluid temperatures, which in turn leads to a slight difference in pressure drop.

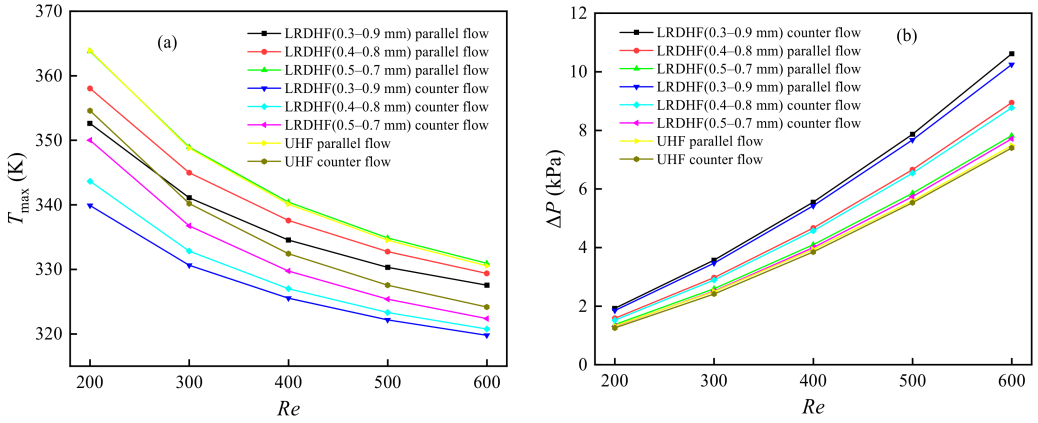


Figure 15. Comparison of the maximum temperature (**a**) and pressure drop (**b**) of the LRDHF model under parallel-flow and counter-flow conditions.

Overall, the LRDHF configuration exhibits a distinctly different trend in absolute mean temperature difference from other fin models, which can be attributed to its fin layout being highly adaptable to counter-flow operating conditions. Compared with parallel-flow configurations, counter-flow operation inherently reduces the peak temperature and elevates the minimum temperature of the channel base. Benefiting from this structural arrangement, the maximum temperature in the midchannel region is further suppressed, thereby effectively improving the overall temperature uniformity. Furthermore, the absolute mean temperature difference in the LRDHF model does not increase monotonically with the reduction in the fin height variation range. Instead, it follows a non-monotonic trend of first decreasing and then increasing, reaching its minimum at a height variation range from 0.4 to 0.8 mm. This finding indicates that, for the LRDHF configuration proposed in this work, the optimal base temperature uniformity can be obtained at a fin height variation range from 0.4 to 0.8 mm.

To objectively evaluate the comprehensive performance of various variable-fin-height models, the widely recognized and commonly employed performance evaluation criterion (*PEC*) is adopted [43],

$$PEC = \frac{Nu/Nu_0}{(f/f_0)^{1/3}}. \tag{16}$$

The subscript "0" denotes the parameters of the reference model, where the UHF configuration is adopted as the baseline. This conventional performance evaluation criterion only incorporates the *Nu* and Δ*P*, failing to characterize the uniformity of temperature in the heat sink. Therefore, the effect of temperature uniformity should be further considered when assessing the comprehensive thermal–hydraulic performance of different fin configurations. As a classical dimensionless index for evaluating the comprehensive behavior of microchannel cooling devices, *PEC* exhibits weak sensitivity to variations in the Reynolds number. As a relative criterion that quantifies the balance between heat transfer augmentation and flow resistance penalty for novel structural designs, *PEC* eliminates the consistent *Re* dependence of *Nu* and the friction factor within the same flow regime. Accordingly, *PEC* primarily reflects the intrinsic structural performance rather than the influence of flow intensity. On this basis, adopting the average *PEC* value over the Reynolds number range from 200 to 600 is reasonable for representing the overall thermal–hydraulic capability of each design.

Figure 16 presents the average *PEC* values of various fin configurations under different fin height variation ranges at $200 \leq Re \leq 600$. Obviously, the LDHF and SDHF configurations yield the highest *PEC*. By contrast, the LRHF and SRHF configurations deliver the lowest *PEC* values, which do not vary significantly with the fin height variation range; the

maximum *PEC* is obtained at a fin height variation range from 0.4 to 0.8 mm. This trend indicates that for fins whose height diminishes downstream, a larger fin height variation range facilitates the attainment of superior *PEC*. In comparison, fins with increasing height along the flow direction exhibit only marginal differences in *PEC* under various height variation conditions. The LRDHF configuration demonstrates moderate *PEC*, which decreases continuously as the fin height variation range narrows. Notably, $PEC < 1$ implies that the corresponding fin configuration possesses inferior thermo-hydraulic performance relative to the conventional UHF design; $PEC > 1$ implies that the thermo-hydraulic performance of the corresponding fin configuration is superior to that of the conventional UHF design.

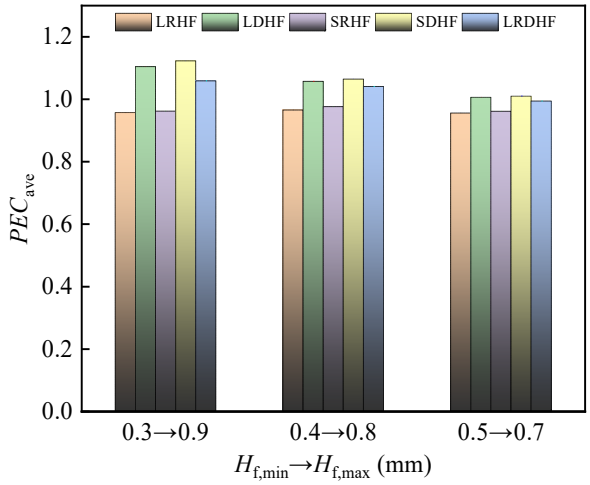


Figure 16. Average *PEC* under different fin height variation ranges.

Following determination of *PEC*, comprehensive performance assessment of various models necessitates consideration of temperature uniformity, quantified as the absolute mean temperature difference for comparative analysis. Employing absolute mean temperature difference in UHF as the baseline, the temperature uniformity of variable-height fin models across various height variation ranges is subsequently discussed. The dimensionless parameter φ is defined as:

$$\varphi = \frac{\Delta T_{m_0} - \Delta T_m}{\Delta T_{m0}}. \quad (17)$$

Obviously, φ represents the relative change in the absolute mean temperature difference of the variable-height fin model with respect to that of the UHF model under identical operating conditions, with subscript 0 denoting the absolute mean temperature difference of the UHF model. It quantifies the improvement in temperature uniformity over the uniform-height fin configuration. $\varphi > 0$ signifies improved temperature uniformity, $\varphi < 0$ shows deteriorated uniformity, and a higher φ indicates a more substantial improvement in temperature uniformity compared to the UHF design.

Figure 17 illustrates the average comprehensive performance index φ_{ave} of various variable-height fin models at $200 \leq Re \leq 600$ under diverse fin height variation ranges. For all investigated configurations except LRDHF, φ decreases monotonically with the reduction in the fin height variation range. In contrast, the LRDHF model achieves its maximum φ at a height variation range from 0.4 to 0.8 mm. This outcome further verifies that the optimal temperature uniformity performance of the LRDHF configuration can be attained at a fin height variation range of approximately 0.4 to 0.8 mm.

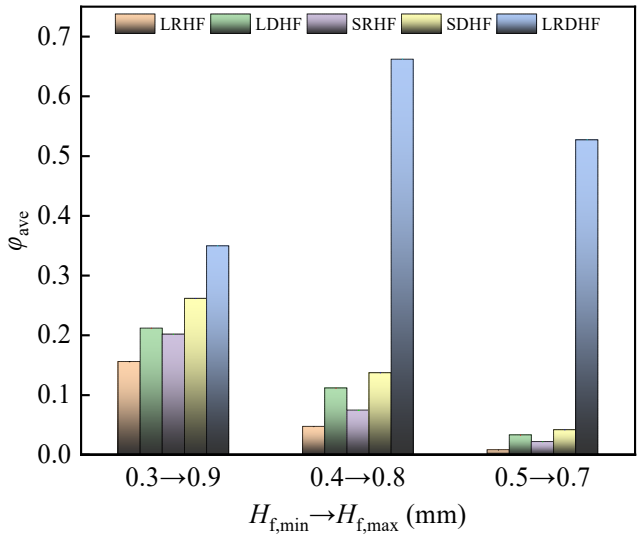


Figure 17. φ_{ave} of all variable-height fin models at $200 \leq Re \leq 600$ under various height variation ranges.

Figure 18 displays the base surface temperature contours of the LRDHF configuration under different fin height variation ranges at Re = 200. The overall base temperature level rises gradually as the fin height variation range decreases, accompanied by an apparent migration of high-temperature regions. The locations of the peak and lowest base surface temperatures are explicitly marked in the contours. Under the maximum fin height variation condition, high-temperature zones develop on both sides of the channel central region. As the fin height variation range decreases, these hot zones gradually migrate toward the channel midsection. This physical phenomenon arises because a reduced fin height variation range renders the variable-height fin geometry progressively closer to the conventional UHF structure.

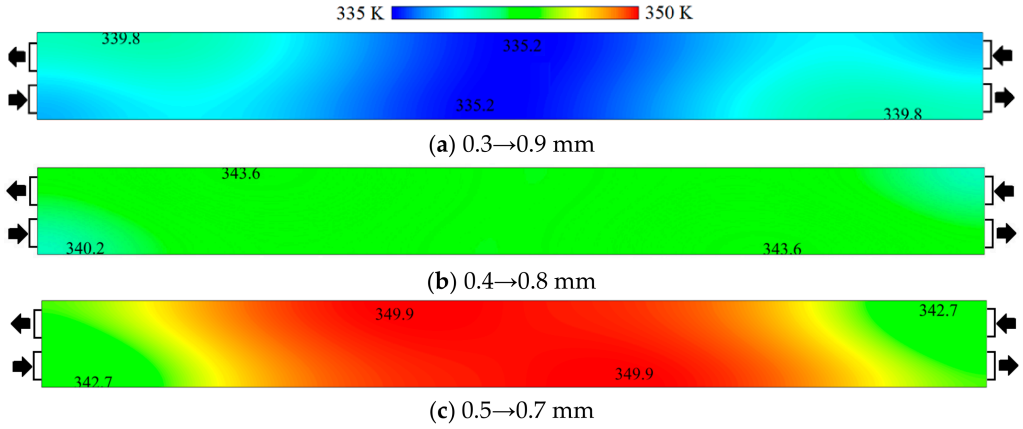


Figure 18. Base surface temperature contours of LRDHF at various fin height variation ranges at Re = 200.

In terms of the *PEC* alone, the SDHF configuration with a height variation range from 0.3 mm to 0.9 mm achieves the optimal performance. Nevertheless, temperature uniformity is equally essential to the practical thermal management performance, necessitating a comprehensive evaluation that integrates both thermal–hydraulic efficiency and temperature uniformity. Despite the superior *PEC* of the SDHF configuration, the LRDHF configuration with a height variation range from 0.4 mm to 0.8 mm delivers the best temperature uniformity among all investigated fin models. Consequently, the LRDHF configuration achieves a better balanced overall performance when both *PEC* and temperature uniformity are

taken into account. Although the SDHF configuration exhibits superior *PEC*, the LRDHF with a fin height variation range of 0.4 → 0.8 mm achieves considerably better temperature uniformity among all investigated fin configurations. According to the calculation results, when both *PEC* and temperature uniformity are considered, the LRDHF shows inferior thermo-hydraulic performance relative to SDHF. However, it features excellent temperature uniformity and yields a lower maximum base surface temperature under identical heat flux and operating conditions. Hence, the LRDHF configuration is more advantageous for scenarios sensitive to peak temperature or requiring high temperature uniformity. Quantitative comparison reveals that the average *PEC* of the SDHF (0.3 → 0.9 mm) configuration is merely 7.92% higher than that of the LRDHF (0.4 → 0.8 mm) counterpart. In contrast, the average temperature uniformity growth rate φ_{ave} of LRDHF exceeds that of SDHF by up to 153.4%. Such a substantial improvement in temperature uniformity, achieved with a negligible sacrifice in *PEC*, indicates that this configuration represents a more promising and preferable design for comprehensive microchannel thermal management in scenarios with high requirements for temperature uniformity.

Among all fin height variation ranges, the LRDHF configuration at 0.4 → 0.8 mm yields a slightly lower maximum base temperature than the 0.3 → 0.9 mm case, which is the minimum value for all investigated models within the 0.4 → 0.8 mm height variation group. Furthermore, the maximum base temperature of LRDHF (0.4 → 0.8 mm) is comparable to that of other models operated at the maximum height variation condition of 0.3 → 0.9 mm. These results reveal that the LRDHF of 0.4 → 0.8 mm undergoes only minor heat transfer performance loss relative to its 0.3 → 0.9 mm counterpart, yet achieves a considerable enhancement in temperature uniformity. Considering the overall comprehensive performance, the LRDHF configuration with 0.4 → 0.8 mm is the best candidate for practical scenarios demanding high temperature uniformity.

3.3. Effect of Geometric Parameters

To further explore the effect of channel width and height on the performance of the LRDHF (0.4 → 0.8 mm) configuration, five distinct width–height combinations are observed under the constraint of identical total heat transfer area to characterize the resultant variations in thermo-hydraulic performance. As depicted in Figure 19, ΔP increases with the reduction in channel width and the increase in channel height at a fixed *Re*. Among all tested configurations, the channel with W = 0.3 mm and H = 1.05 mm yields the maximum ΔP, which exhibits a more pronounced increment with increasing *Re*. In comparison, the channel with W = 0.7 mm and H = 0.85 mm presents the minimum pressure drop with a relatively mild growth trend as *Re* increases. This is due to the smaller hydraulic diameter of narrow and tall channel structures, which induces a higher flow velocity at the same *Re*. Furthermore, the enlarged sidewall surface area intensifies the shear stress at the fluid–solid interface, thereby increasing the overall flow resistance and eventually resulting in a higher ΔP.

Figure 20 illustrates the base surface temperature contours of various channel configurations at *Re* = 200 at the same operating conditions. The contour results indicate that the average base surface temperature rises with increasing channel width and decreasing channel height. A sharp elevation in the bottom surface temperature is observed when the channel width exceeds 0.4 mm, demonstrating that channel geometric dimensions significantly affect the heat dissipation performance under the constraint of a constant heat transfer area.

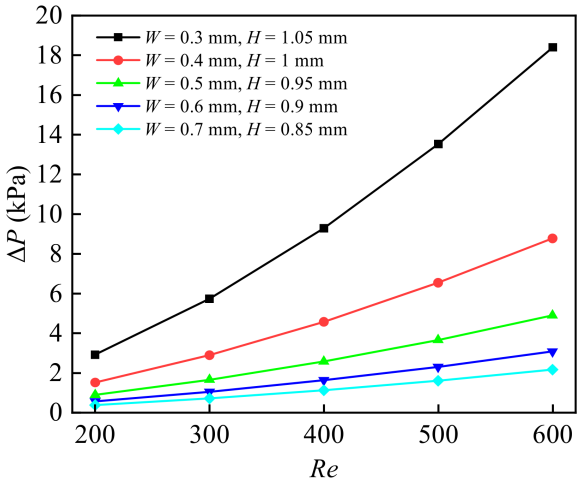
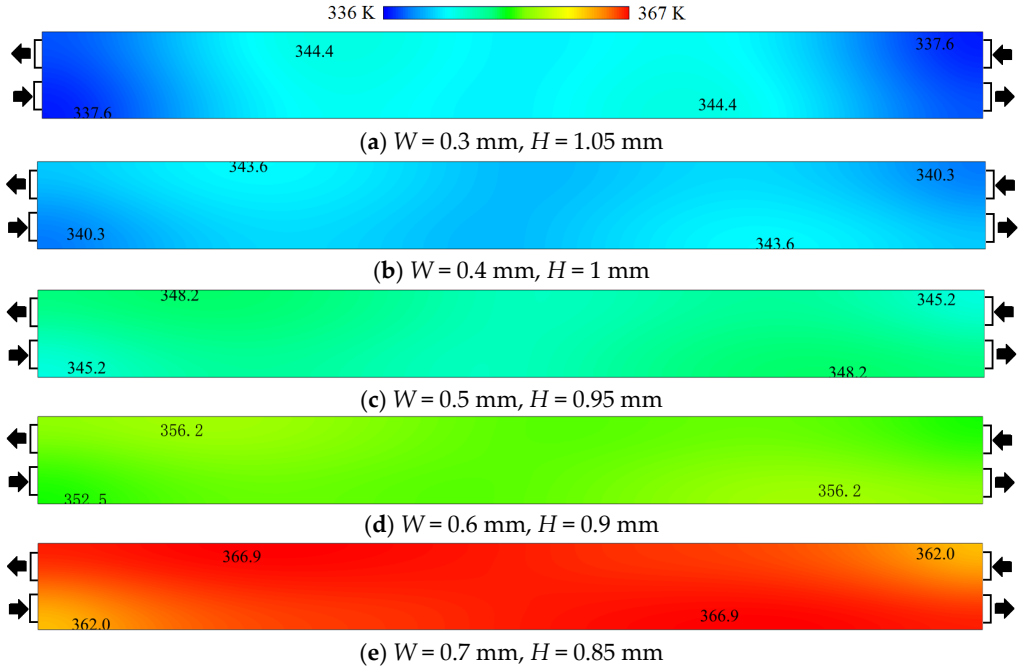


Figure 19. Pressure drops for different heights and widths of channels.



(**a**) W = 0.3 mm, H = 1.05 mm

(**b**) W = 0.4 mm, H = 1 mm

(**c**) W = 0.5 mm, H = 0.95 mm

(**d**) W = 0.6 mm, H = 0.9 mm

(**e**) W = 0.7 mm, H = 0.85 mm

Figure 20. Temperature contour on the base surface for LRDHF (0.4 → 0.8 mm) at Re = 200. It should be noted that these figures are not strictly drawn to scale but maintain the same layout dimensions.

Figure 21a reveals that channels with a smaller width and larger height yield a lower maximum base temperature. Configurations with W = 0.3 mm, H = 1.05 mm and W = 0.4 mm, H = 1.0 mm exhibit nearly identical maximum base temperatures. Nevertheless, a further increase in channel width triggers a notable rise in the peak base temperature. With a fixed total heat transfer area, an increase in channel width accompanied by a decrease in channel height results in a larger hydraulic diameter. At a constant inlet Re, such geometric variation reduces the inlet flow velocity and thereby weakens the convective heat transfer. Consequently, wider and thinner channels produce higher maximum base temperatures under identical operating conditions.

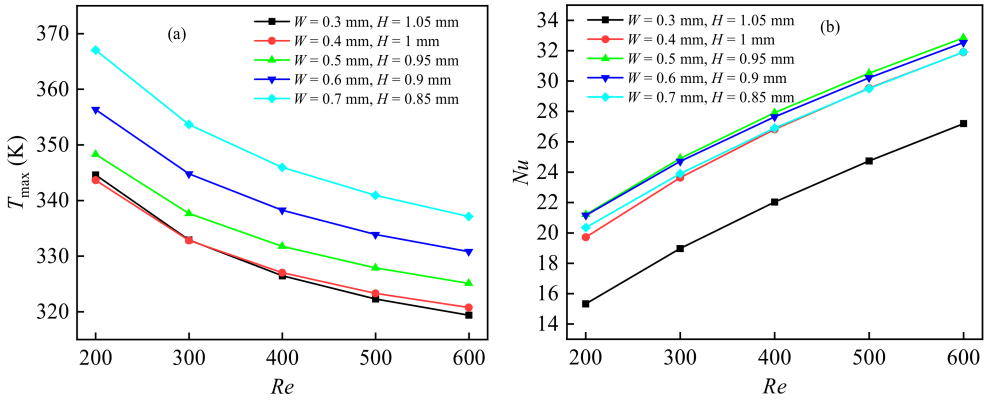


Figure 21. The maximum base surface temperature (**a**) and *Nu* (**b**) for different heights and widths of channels.

Figure 21b presents the Nusselt numbers for the various geometric combinations. It is observed that the variation in *Nu* with the aspect ratio does not follow the same trend as that of T_{max}. Except for the case with W = 0.3 mm and H = 1.05 mm, the *Nu* values for the other configurations are relatively close to one another. Although this specific geometry yields the lowest maximum bottom temperature, it simultaneously exhibits the smallest *Nu*. This discrepancy arises from its smaller hydraulic diameter, which counterbalances the enhanced convective heat transfer and leads to a reduced *Nu*.

Figure 22 shows that the absolute mean temperature difference on the base surface generally decreases with decreasing channel width and increasing height. The channel configuration with W = 0.3 mm and H = 1.05 mm presents a relatively high absolute mean temperature difference at low *Re*. This value gradually declines as *Re* increases, reaching a minimum at *Re* = 600 and continuing to decrease at higher *Re*. For other examined channel geometries, the absolute mean temperature difference decreases steadily and mildly as *Re* rises. This phenomenon is due to the larger hydraulic diameter of wider and thinner channels, which results in a less pronounced increase in flow velocity with growing *Re* and thereby only a moderate improvement in temperature uniformity. In contrast, narrow and tall channels feature smaller hydraulic diameters, leading to a more significant rise in flow velocity with increasing *Re* and a faster enhancement in thermal uniformity. Accordingly, the absolute mean temperature difference in narrow and tall channels declines more rapidly with *Re.* At *Re* = 500, this index becomes comparable to or slightly lower than that of other configurations, and a substantially lower value is achieved at *Re* = 600.

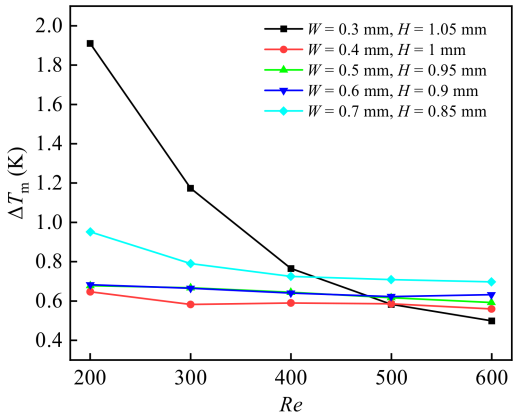


Figure 22. Absolute mean temperature differences in the base surface for LRDHF (0.4 → 0.8 mm) with various dimensions at 200 ≤ *Re* ≤ 600.

3.4. Correlations for Flow Resistance and Heat Transfer

Based on the above analysis, variations in channel cross-sectional width-to-height ratio and fin height variation rate exert influences on flow resistance and thermal performance. Accordingly, two parameters, the aspect ratio α of the channel and the fin height variation ratio η, are introduced,

$$\alpha = \frac{W}{H},\ \eta = \frac{H_{\mathrm{f,max}} - H_{\mathrm{f,min}}}{H_{\mathrm{f,min}}}. \tag{18}$$

Based on the calculated data, the correlation of the friction factor (f) for the LRDHF configuration was fitted as:

$$f = 3.4Re^{-0.431}\eta^{0.184}\exp(-0.787\alpha), \tag{19}$$

where the coefficient of determination (R^2) exceeds 0.95, the mean relative error is within 7%, and the maximum relative error does not exceed 10%.

Similarly, the heat transfer correlation for the LRDHF configuration was expressed as:

$$Nu = 17.1Re^{0.422}\eta^{0.092}(1 + 15.026\alpha - 12.168\alpha^2), \tag{20}$$

where the coefficient of determination (R^2) exceeds 0.95, the mean relative error is below 4%, and the maximum relative error is within 8%.

The applicable ranges of Equations (19) and (20) are $200 \leq Re \leq 600$, $0.4 \leq \eta \leq 2$, and $0.286 \leq \alpha \leq 0.824$. It should be noted that these correlations are derived from the present numerical data and are intended for preliminary design estimates within these parameter bounds. Further experimental and numerical studies are required to extend their applicability to broader ranges of Re, η, and α.

Figure 23 shows the comparison between the fitted and predicted values of the Nusselt number (a) and the friction factor (b). It can be seen that the fitted values are in good agreement with the calculated values. The number of fitting samples for both the Nusselt number and the friction factor is 40. Due to the limited sample size, the correlations are only applicable to the LRDHF (0.4–0.8 mm) model proposed in this work, with water as the working fluid.

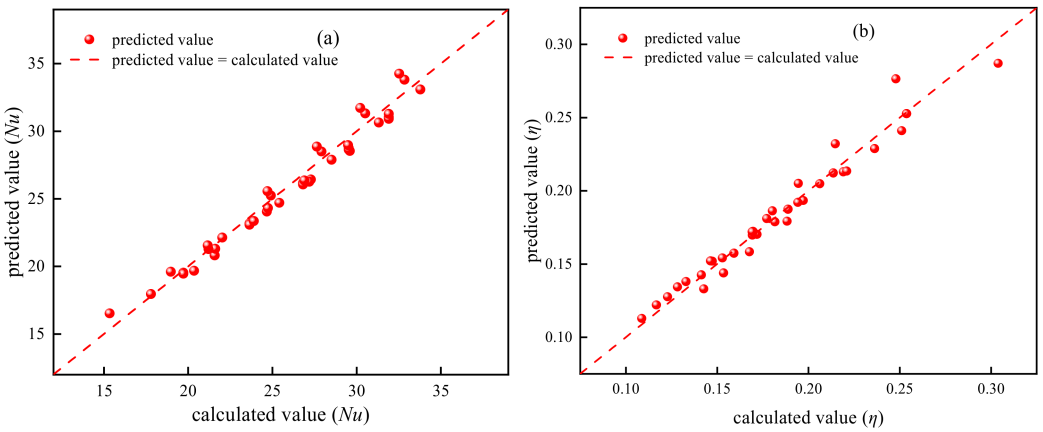


Figure 23. Comparison of the fitted and predicted values of the Nusselt number (**a**) and friction factor (**b**).

4. Conclusions

This paper numerically investigated the thermal and hydraulic performance of microchannel heat sinks with a streamwise variable-height fin configuration under the counter-flow model. The main conclusions are listed as follows:

(1) In contrast to the parallel-flow arrangement, the counter-flow configuration achieves a centrosymmetric temperature distribution with the hot spot located in the central region, which reduces the maximum base temperature and enhances temperature uniformity, rendering the counter-flow microchannel heat sink more suitable for applications demanding precise thermal management.

(2) At a fixed total heat transfer area, all variable-height fin configurations exhibit lower maximum base temperatures and improve base temperature uniformity compared with the UHF design. Nevertheless, this thermal improvement comes with an increased ΔP, which arises from repeated flow contraction and expansion as well as vortex generation in the inter-fin regions.

(3) Among the five variable-height fin configurations, the LRDHF achieves the minimum peak base temperature and absolute average temperature difference across all fin height ranges. When only the *PEC* is compared, the SDHF configuration with a fin height variation range of $0.3 \rightarrow 0.9$ mm yields the maximum *PEC* and optimal thermo-hydraulic performance. However, the LRDHF (0.4–0.8 mm) model achieves temperature uniformity far superior to that of the other models while maintaining a relatively small gap in average PEC. Therefore, for scenarios with high temperature uniformity requirements, LRDHF (0.4–0.8 mm) is a better choice.

(4) At a fixed heat transfer area, variations in channel width and height significantly impact the thermal and hydraulic performance. Increasing the channel width while decreasing the channel height results in a rise in the maximum base temperature and a deterioration in base temperature uniformity, albeit with a reduction in ΔP.

(5) Based on the numerical results, highly accurate empirical relations for the friction factor and Nusselt number are developed for the LRDHF configuration considered in this work.

Author Contributions: Conceptualization, C.-Q.H. and Y.-R.L.; methodology, C.-Q.H., J.-J.Y. and Y.-R.L.; software, C.-Q.H.; validation, C.-Q.H. and Y.-R.L.; formal analysis, C.-Q.H.; investigation, C.-Q.H., J.-J.Y. and C.-M.W.; resources, C.-Q.H. and C.-M.W.; data curation, C.-Q.H.; writing—original draft preparation, C.-Q.H.; writing—review and editing, C.-M.W. and Y.-R.L.; visualization, C.-Q.H.; supervision, C.-M.W. and Y.-R.L.; project administration, Y.-R.L.; funding acquisition, Y.-R.L. All authors have read and agreed to the published version of the manuscript.

Funding: This research was funded by National Natural Science Foundation of China, grant number 52076017.

Data Availability Statement: The data presented in this study are available on reasonable request from the corresponding author.

Conflicts of Interest: The authors declare no conflicts of interest.

References

1. Xia, G.D.; Jiang, J.; Wang, J.; Zhai, Y.L.; Ma, D.D. Effects of different geometric structures on fluid flow and heat transfer performance in microchannel heat sinks. *Int. J. Heat Mass Transf.* **2015**, *80*, 439–447. [CrossRef]
2. Alteneiji, M.; Raafat, A.; Alnuaimi, S.K. Impact of height and secondary flow patterns of circle, square and triangle shaped pin fins on microchannel heat sinks performance. *Therm. Sci. Eng. Prog.* **2025**, *67*, 104166. [CrossRef]
3. Madi, K.; Raafat, A.; Al Nuaimi, S. Enhanced thermal management in microelectronic cooling: A study on pairing multiple pin-fin shapes in microchannel heat sinks. *Int. J. Thermofluids* **2025**, *28*, 101283. [CrossRef]
4. Alam, T.; Ansari, M.M.; Kulkarni, K.S.; Ali, N.; Haque, I. Investigating tetragonal prismatic pin-fins in microchannel heat sinks: Optimizing cooling performance. *Therm. Sci. Eng. Prog.* **2025**, *64*, 103816. [CrossRef]
5. Hou, X.L.; Yang, Y.H. A novel hybrid staggered arrangement petal-shaped pin-fin microchannel heat sink for hotspot mitigation. *Appl. Therm. Eng.* **2026**, *291*, 130079. [CrossRef]
6. Ali, S.; Ahmad, F.; Akhtar, K.; Habib, N.; Aamir, M.; Giasin, K.; Vafadar, A.; Pimenov, D.Y. Numerical investigation of microchannel heat sink with trefoil shape ribs. *Energies* **2021**, *14*, 6764. [CrossRef]

7. Li, Y.T.; Yang, Y.X.; Gong, L.; Cui, W.S.; Yang, B.Y. Design of biomimetic wheat-grain-shaped pin fins for enhanced heat transfer in microchannel heat sink. *Appl. Therm. Eng.* **2025**, *284*, 129074. [CrossRef]
8. Tanzim, R.; Das, A.; Zaman, S.N.; Lia, T.A.; Sarwar, S.T. A chromosome inspired fin structure for microchannel heat sinks: CFD driven XGBR, ANN, and MLR models for thermal and fluid flow prediction. *Int. Commun. Heat Mass Transf.* **2025**, *169*, 109763. [CrossRef]
9. Wang, C.; Zhang, F.R.; Zhao, Q.L.; Xin, L.Q.B.; Zhao, H. Whale optimization algorithm for enhancing thermal performance of bionic lemon-slice microchannel-fin composite heat sink. *Int. J. Heat Fluid Flow* **2026**, *120*, 110335. [CrossRef]
10. Wang, J.L.; Qi, S.H.; Yu, X. Numerical investigations of the thermal-hydraulic characteristics of microchannel heat sinks inspired by leaf veins. *Energies* **2024**, *17*, 311. [CrossRef]
11. Khtar, K.; Ali, H.; Ud Din, I.; Abbas, A.; Zahir, M.Z.; Ahmad, F.; Alam, F.; Shah, N.; Aamir, M. Heat transfer augmentation and entropy generation analysis of microchannel heat sink (MCHS) with symmetrical ogive-shaped ribs. *Energies* **2023**, *16*, 2783. [CrossRef]
12. Yuan, J.; Deng, N.K.; Qu, Y.F.; Du, L.; Hu, W.B.; Zhang, Z.Y.; Wang, H.X. A novel center-hybrid pin-fin microchannel heat sink with embedded secondary microchannels for hotspot thermal management. *Int. J. Therm. Sci.* **2025**, *207*, 109381. [CrossRef]
13. Chen, S.Y.; Liu, Z.W.; Wang, B.Y.; Li, P. Heat transfer enhancement and temperature uniformity improvement of microchannel heat sinks with twisted blade-like fins. *Case Stud. Therm. Eng.* **2023**, *52*, 103788. [CrossRef]
14. Vasilev, M.P.; Abiev, R.S.; Kumar, R. Effect of circular pin-fins geometry and their arrangement on heat transfer performance for laminar flow in microchannel heat sink. *Int. J. Therm. Sci.* **2021**, *170*, 107177. [CrossRef]
15. Thanikodi, S.; Saravanan, R. Shape optimized pin-fin heat sink design for efficient thermal management in microelectronics: A simulation-based approach supporting SDG-driven innovation. *Results Eng.* **2025**, *29*, 108786. [CrossRef]
16. Rehman, M.M.U.; Cheema, T.A.; Ahmad, F.; Khan, M.; Abbas, A. Thermodynamic assessment of microchannel heat sinks with novel sidewall ribs. *J. Thermophys. Heat Transf.* **2020**, *34*, 243–254. [CrossRef]
17. Chai, L.; Xia, G.D.; Wang, H.S. Laminar flow and heat transfer characteristics of interrupted microchannel heat sink with ribs in the transverse microchambers. *Int. J. Therm. Sci.* **2016**, *110*, 1–11. [CrossRef]
18. Zhu, Q.F.; Su, R.R.; Xia, H.X.; Zeng, J.W.; Chen, J.J. Title of the paper, Numerical simulation study of thermal and hydraulic characteristics of laminar flow in microchannel heat sink with water droplet cavities and different rib columns. *Int. J. Therm. Sci.* **2022**, *172*, 107319. [CrossRef]
19. Zhu, Q.F.; Jin, Y.Y.; Chen, J.J.; Su, R.R.; Zhu, F.Y.; Li, H.X.; Wan, J.F.; Zhang, H.W.; Sun, H.L.; Cui, Y.; et al. Computational study of rib shape and configuration for heat transfer and fluid flow characteristics of microchannel heat sinks with fan-shaped cavities. *Appl. Therm. Eng.* **2021**, *195*, 117171. [CrossRef]
20. Lu, G.F.; Yang, J.R.; Zhai, X.Q.; Wang, X.L. Hotspot thermal management in microchannel heat sinks with vortex generators. *Int. J. Therm. Sci.* **2021**, *161*, 106727. [CrossRef]
21. Abdollahi, A.; Shams, M. Optimization of shape and angle of attack of winglet vortex generator in a rectangular channel for heat transfer enhancement. *Appl. Therm. Eng.* **2015**, *81*, 376–387. [CrossRef]
22. Shi, X.J.; Li, S.; Mu, Y.J.; Yin, B.T. Geometry parameters optimization for a microchannel heat sink with secondary flow channel. *Int. Commun. Heat Mass Transf.* **2019**, *104*, 89–100. [CrossRef]
23. Sabzpoushan, S.; Sabouri, M. Secondary flow through lateral passages to improve hydrothermal performance of liquid-cooled microchannel heat sinks. *Appl. Therm. Eng.* **2023**, *227*, 120009. [CrossRef]
24. Shen, H.; Wang, C.C.; Xie, G.N. A parametric study on thermal performance of microchannel heat sinks with internally vertical bifurcations in laminar liquid flow. *Int. J. Heat Mass Transf.* **2018**, *117*, 487–497. [CrossRef]
25. Feng, S.; Yan, Y.F.; Li, H.J.; He, Z.Q.; Zhang, L. Temperature uniformity enhancement and flow characteristics of embedded gradient distribution micro pin fin arrays using dielectric coolant for direct intra-chip cooling. *Int. J. Heat Mass Transf.* **2020**, *156*, 119675. [CrossRef]
26. Shi, Z.R.; Lan, X.; Cao, J.; Zhao, N.; Cheng, Y. Numerical study of variable density and height flow guided pin fin in an open microchannel heat sink. *Int. J. Heat Mass Transf.* **2024**, *225*, 125405. [CrossRef]
27. Li, X.; Lan, X.; Wang, X.H.; Xin, G.M.; Cheng, Y. Flow and thermal analysis of manifold jet impingement microchannel heat sink featuring low pressure drop and high temperature uniformity. *Appl. Therm. Eng.* **2024**, *302*, 131940.
28. Li, Z.X.; Wang, Q.; Gao, Y.F.; Zhang, L.N.; Liu, X.Q. Synergistic mechanism of hydrothermal performance and temperature uniformity in microchannel heat sink with non-uniformly distributed drop-shaped fins. *Int. J. Therm. Sci.* **2026**, *222*, 110524. [CrossRef]
29. Kumar, R.; Pandey, M. Numerical investigations on the effect of fin thickness on thermal performance characteristics of microchannel heat sinks. *Int. Commun. Heat Mass Transf.* **2026**, *177*, 111486. [CrossRef]
30. Sallar, H.; Irfan, M.; Khan, M.M.; Shahzad, M.W. Hydro-thermal performance of an I-shaped pin fin microchannel heat sink with variable pin fin height, thickness and orientation. *Int. Commun. Heat Mass Transf.* **2025**, *160*, 108256. [CrossRef]

31. Atci, F.; Markal, B.; Evcimen, A. Influence of regional artificial cavity layouts on flow boiling in micro heat sinks with stepwise-decreasing pin-fin heights. *Int. Commun. Heat Mass Transf.* **2027**, *273*, 129693. [CrossRef]
32. Godi, N.Y. Novel cooling approach in microchannel with fixed and variable fins configuration. *Int. J. Therm. Sci.* **2026**, *220*, 110276. [CrossRef]
33. Shen, H.; Zhang, Y.C.; Wang, C.C.; Xie, G.N. Comparative study for convective heat transfer of counter-flow wavy double-layer microchannel heat sinks in staggered arrangement. *Appl. Therm. Eng.* **2018**, *137*, 228–237. [CrossRef]
34. Tikadar, A.; Paul, T.C.; Oudah, S.K.; Abdulrazzaq, N.M.; Salman, A.S.; Khan, J.A. Enhancing thermal-hydraulic performance of counter-flow mini-channel heat sinks utilizing secondary flow: Numerical study with experimental validation. *Int. Commun. Heat Mass Transf.* **2020**, *111*, 104447. [CrossRef]
35. Tikadar, A.; Oudah, S.K.; Paul, T.C.; Salman, A.S.; Morshed, A.K.M.M.; Khan, J.A. Parametric study on thermal and hydraulic characteristics of inter-connected parallel and counter flow mini-channel heat sink. *Appl. Therm. Eng.* **2019**, *153*, 15–28. [CrossRef]
36. Abdallah, Y.M.A.; Essam, M.A.Z.; Elqady, H.I.; Rabie, M.; Elkady, M.F.; Ookawara, S.; El-Shazly, A.H.; Radwan, A. Thermal analysis of high concentrator photovoltaic module using convergent-divergent microchannel heat sink design. *Appl. Therm. Eng.* **2021**, *183*, 116201. [CrossRef]
37. Khoshvaght-Aliabadi, M.; Abbaszadeh, A.; Rashidi, M.M. Comparison of co-and counter-current modes of operation for wavy minichannel heat sinks. *Int. J. Therm. Sci.* **2022**, *171*, 107189. [CrossRef]
38. Ma, L.K.; Zhu, H.; Ding, Y.Y.; Jin, Q. Thermal performance of microchannel heat sink with interrupted and non-uniform width channel. *Appl. Therm. Eng.* **2025**, *283*, 129002. [CrossRef]
39. Chakma, A.; Tikadar, A. Hybrid microchannel heat sink using tapered channels and interconnectors for microelectronics cooling. *Appl. Therm. Eng.* **2025**, *285*, 129156. [CrossRef]
40. Kumar, R.; Pandey, M. Numerical analysis of heat transfer and fluid flow characteristics of microchannel heat sinks with streamwise variation of fin height. *Int. Commun. Heat Mass Transf.* **2025**, *163*, 108706. [CrossRef]
41. Qu, W.L.; Mudawar, I. Experimental and numerical study of pressure drop and heat transfer in a single-phase micro-channel heat sink. *Int. J. Heat Mass Transf.* **2002**, *45*, 2549–2565. [CrossRef]
42. Wang, G.L.; Wang, Z.C.; Lai, L.Y.; Xie, D.D.; Zhu, Y.; Ding, G.D.; Xu, Q. Experimental and numerical investigation of hydrothermal performance of a microchannel heat sink with pin fins. *Case Stud. Therm. Eng.* **2024**, *60*, 104631. [CrossRef]
43. Zhai, Y.L.; Xia, G.D.; Liu, X.F.; Li, Y.F. Exergy analysis and performance evaluation of flow and heat transfer in different micro heat sinks with complex structure. *Int. J. Heat Mass Transf.* **2015**, *84*, 293–303. [CrossRef]

Disclaimer/Publisher's Note: The statements, opinions and data contained in all publications are solely those of the individual author(s) and contributor(s) and not of MDPI and/or the editor(s). MDPI and/or the editor(s) disclaim responsibility for any injury to people or property resulting from any ideas, methods, instructions or products referred to in the content.